AGU PUBLICATIONS

JGR

Journal of Geophysical Research: Atmospheres

RESEARCH ARTICLE

10.1002/2013JD021170

**Key Points:**
- VIIRS capabilities combine the best aspects of heritage instrumentation
- NCC Imagery issues have largely been resolved
- VIIRS provides impressive multispectral imagery for a wide range of users

**Correspondence to:**
D. Hillger,
Don.Hillger@NOAA.gov

**Citation:**
Hillger, D., C. Seaman, C. Liang, S. Miller, D. Lindsey, and T. Kopp (2014), Suomi NPP VIIRS Imagery evaluation, *J. Geophys. Res. Atmos.*, *119*, 6440–6455, doi:10.1002/2013JD021170.

Received 12 NOV 2013
Accepted 8 MAY 2014
Accepted article online 13 MAY 2014
Published online 10 JUN 2014

# Suomi NPP VIIRS Imagery evaluation

**Donald Hillger[1], Curtis Seaman[2], Calvin Liang[3], Steven Miller[2], Daniel Lindsey[1], and Thomas Kopp[4]**

[1]NOAA Center for Satellite Applications and Research, Fort Collins, Colorado, USA, [2]CIRA, Colorado State University, Fort Collins, Colorado, USA, [3]Northrop Grumman Aerospace Systems, Redondo Beach, California, USA, [4]Aerospace Corporation, El Segundo, California, USA

**Abstract** The Visible Infrared Imaging Radiometer Suite (VIIRS) combines the best aspects of both civilian and military heritage instrumentation. VIIRS has improved capabilities over its predecessors: a wider swath width and much higher spatial resolution at swath edge. The VIIRS day-night band (DNB) is sensitive to very low levels of visible light and is capable of detecting low clouds, land surface features, and sea ice at night, in addition to light emissions from both man-made and natural sources. Imagery from the Suomi National Polar-orbiting Partnership (Suomi NPP) satellite has been in the checkout process since its launch on 28 October 2011. The ongoing evaluation of VIIRS Imagery helped resolve several imagery-related issues, including missing radiance measurements. In particular, near-constant contrast imagery, derived from the DNB, had a large number of issues to overcome, including numerous missing or blank-fill images and a stray light leakage problem that was only recently resolved via software fixes. In spite of various sensor issues, the VIIRS DNB has added tremendous operational and research value to Suomi NPP. Remarkably, it has been discovered to be sensitive enough to identify clouds even in very low light new moon conditions, using reflected light from the Earth's airglow layer. Impressive examples of the multispectral imaging capabilities are shown to demonstrate its applications for a wide range of operational users. Future members of the Joint Polar Satellite System constellation will also carry and extend the use of VIIRS. Imagery evaluation will continue with these satellites to ensure the quality of imagery for end users.

## 1. Introduction

Visible Infrared Imaging Radiometer Suite (VIIRS) Imagery is the most basic VIIRS-based environmental data record (EDR) product available from the Suomi National Polar-orbiting Partnership (S-NPP) satellite [*Hillger et al.*, 2013]. (Other atmospheric, land, and ocean EDRs are not covered here.) Satellite imagery enables weather analysts/forecasters to discern and interpret environmental phenomena (either manually or automatically). The Imagery EDRs, which are derived from the VIIRS sensor data records (SDRs), may also be input to remote sensing algorithms which derive quantitative data products for various geophysical features, ranging from ocean eddies to high-level thin cirrus. However, those quantitative products are not the focus of this article. Rather, VIIRS Imagery is examined from the perspective of its basic performance and improvements upon heritage satellite instrumentation to which it can be directly compared.

The performance of VIIRS Imagery EDRs across the visible, near-infrared, and infrared portion of the spectrum is a key attribute, considered critical for the success of VIIRS on S-NPP. Performance requirements for VIIRS Imagery are specified in the Joint Polar Satellite System (JPSS) requirements documents, which can be found online [*Level 1 Requirements Document* (*L1RD*), 2013; *L1RD Supplement*, 2013]. The requirements apply to six of the current 12 Imagery EDRs (see Table 1), a result of their specific use by the Alaskan National Weather Service. For example, VIIRS I band imagery has a nadir horizontal resolution requirement of 400 m across the entire operating temperature range, as well as an 800 m resolution at edge of swath. Other requirements for imagery are more qualitative. As an example, a specification/requirement for VIIRS Imagery is the ability to do "manual interpretation" of sea ice extent, concentration, and ice edges in multispectral imagery, facilitated by use of false color composite images of the VIIRS reflectance and brightness temperature bands [*Imagery Calibration/Validation Plan*, 2009]. These capabilities are illustrated herein.

The following sections provide a description of the S-NPP spacecraft and an introduction to VIIRS Imagery, improvements with VIIRS over its predecessors, the identification and correction of imagery issues, the production of NCC from DNB imagery, and a survey of VIIRS Imagery showing its high quality and usefulness for analysis of many types of atmospheric and land surface phenomena.


©2014. American Geophysical Union. All Rights Reserved.

**Table 1.** VIIRS Bands and Explanations[a]

| VIIRS Band | Central Wavelength (μm) | Wavelength Range (μm) | Band Explanation | Spatial Resolution (m) at Nadir |
|---|---|---|---|---|
| M1[c] | 0.412[c] | 0.402–0.422[c] | Visible | 750 m |
| M2 | 0.445 | 0.436–0.454 | | |
| M3[d] | 0.488 | 0.478–0.488 | | |
| M4[c,d] | 0.555[c] | 0.545–0.565[c] | | |
| M5[d] (B) | 0.672 | 0.662–0.682 | | |
| M6 | 0.746 | 0.739–0.754 | Near IR | |
| M7 (G) | 0.865 | 0.846–0.885 | | |
| M8 | 1.240 | 1.23–1.25 | Shortwave IR | |
| M9[c] | 1.378[c] | 1.371–1.386[c] | | |
| M10 (R) | 1.61 | 1.58–1.64 | | |
| M11 | 2.25 | 2.23–2.28 | | |
| M12 | 3.7 | 3.61–3.79 | Medium-wave IR | |
| M13 | 4.05 | 3.97–4.13 | | |
| M14[b] | 8.55[b] | 8.4–8.7[b] | Longwave IR | |
| M15[b] | 10.763[b] | 10.26–11.26[b] | | |
| M16[b] | 12.013[b] | 11.54–12.49[b] | | |
| DNB[c] | 0.7[c] | 0.5–0.9[c] | Visible | 750 m across full scan |
| I1[b] (B) | 0.64[b] | 0.6–0.68[b] | Visible | 375 m |
| I2[c] (G) | 0.865[c] | 0.85–0.88[c] | Near IR | |
| I3[c] (R) | 1.61[c] | 1.58–1.64[c] | Shortwave IR | |
| I4[b] | 3.74[b] | 3.55–3.93[b] | Medium-wave IR | |
| I5[b] | 11.45[b] | 10.5–12.4[b] | Longwave IR | |

[a]M = Moderate resolution bands; I = Imagery resolution bands. M band and I band components of natural color imagery are noted with R, G, and B.
[b]Bands that are specifically required Imagery EDRs.
[c]Other Imagery EDRs.
[d]Components of true color visible imagery.

## 2. Suomi NPP and VIIRS Imagery

S-NPP was launched on 28 October 2011 marking a new generation of operational polar-orbiting spacecraft. Originally named for the NPOESS (National Polar-orbiting Operational Environmental Satellite System) Preparatory Project [*Lee et al.*, 2010], but with the cancellation of the NPOESS program, the "NPP" acronym was changed in January 2012 to "Suomi National Polar-orbiting Partnership" to honor "The father of satellite meteorology," Verner Suomi [*Lewis et al.*, 2010]. S-NPP serves a dual role as both operational system and risk-reduction satellite within the context of the future Joint Polar Satellite System (JPSS) series, with JPSS 1 and 2 to be launched in the next several years.

VIIRS covers the entire Earth twice daily at about 0130 and 1330 local time. The first VIIRS visible images from S-NPP became available on 21 November 2011, less than a month after launch of the satellite. (Instrument turn-on typically follows the initial spacecraft checkout and outgassing so as not to contaminate the imaging optics.) Infrared bands followed on 19 January 2012. VIIRS images have high spatial resolution (750 m at nadir and maximum of 1600 m globally, for the M bands; 375 m at nadir and finer than 800 m globally, for the I bands and DNB) and multispectral (22 band) capabilities, unlike those from the Moderate Resolution Imaging Spectroradiometer (MODIS), a key heritage instrument aboard the NASA Earth Observing System Terra and Aqua satellites.

VIIRS includes an expanded set of 22 visible and infrared spectral bands (Table 1) that greatly improves the spectral coverage of its operational predecessor, the NOAA advanced very high resolution radiometer (AVHRR), as well as an enhanced capability day-night band (DNB) [*Lee et al.*, 2006] to improve upon the low-light nighttime visible imagery available from the Operational Linescan System (OLS) on the Defense Meteorological Satellite System (DMSP) series.

VIIRS SDRs are parsed into single-band granules containing approximately 86 s of data consisting of 48 cross-track scans. Each scan employs either 16 or 32 detectors depending on the detector resolution (M and I band, respectively) and position along the scan line, resulting in either 768 or 1536 scan lines per granule. Due to the high spatial resolution and wide swath and the number of bands, including two different


©2014. American Geophysical Union. All Rights Reserved.

resolutions, and both SDR and EDR file types, including the geolocation information, VIIRS Imagery products can add up to 2 Gb of data per granule.

For the DNB, the spatial resolution is similar to that of the M bands but with more pixels per scan line. The actual detector pixels are skillfully aggregated at different locations along the scan to create a pixel size that is nearly the same at swath edge as at nadir. Details of the pixel aggregation are available in the VIIRS documentation [*Imagery Algorithm Theoretical Basis Document* (*ATBD*), 2011]. However, when the DNB is turned into NCC EDRs, the mapping is the same as that of the M band Imagery.

The VIIRS SDRs require image processing software to turn the granules into remapped and gap-filled Imagery EDRs. For the non-NCC bands, the EDRs are merely SDRs remapped into a Ground Track Mercator (GTM) grid, where one axis of the grid lies along the satellite subtrack and cross-track elements are perpendicular to the satellite track. For these bands, the EDR Imagery is produced by moving radiances from their SDR locations to the nearest GTM location, with no change in the quantitative values [*Imagery ATBD*, 2011]. The main advantage, however, is that gaps in the SDRs, due to intentional deletions in the SDRs at higher scan angles meant to reduce bow tie effects, are filled in the Imagery EDRs. The exception is the DNB, which is transformed into near-constant contrast (NCC) imagery when remapped. The name change is accompanied by a process that creates a more user-friendly product through manipulation of the multiple-gain DNB radiances into a "pseudo-albedo" product, as are explained in section 5.1.

Before showing imagery examples, note from Table 1 that only six of the M bands are currently available as Imagery EDRs. However, the choice of the six M band Imagery EDRs is supposed to be flexible, to change upon user request. In order to allow this capability, all M bands have been successfully turned into Imagery EDRs in offline processing, as part of the imagery checkout. The default choice of M band Imagery EDRs is not considered optimal by the Imagery Team and in particular does not allow the production of true color imagery. Because all M bands can potentially be made into Imagery EDRs, some of the imagery examples shown are produced from other than the default set of M bands Imagery EDRs. The Imagery Team recommends that all 16 M bands be turned into Imagery EDRs. The 10 additional M band Imagery EDRs would result in only a 2% increase in the data volume associated with SDRs and current Imagery EDRs.

As introductory examples of the quality of VIIRS Imagery, Figure 1a shows a "natural color" red-green-blue (RGB) image combination [*Lensky and Rosenfeld*, 2008], in this case a combination of VIIRS bands M10 (1.61 μm), M7 (0.865 μm), and M5 (0.672 μm), respectively, at 750 m spatial resolution. (The same product is also available from the equivalent I bands but not shown here.) This combination of bands on the Spinning Enhanced Visible and Infrared Imager sensor is a featured imagery product from Meteosat Second Generation. Natural color imagery is very useful for discriminating various types of ground cover (vegetated versus not) and cloud types (liquid versus ice). Rayleigh correction is not applied to natural color imagery, simplifying its generation, compared to true color imagery which is typically Rayleigh corrected to reduce atmospheric scattering effects. Similarly, in Figure 1b, VIIRS Imagery is shown to be useful in detecting sea ice extent and ice edges. In this case the natural color image is created from VIIRS bands I3 (1.61 μm), I2 (0.865 μm), and I1 (0.64 μm), respectively, at 375 m spatial resolution.

## 3. Improvements With VIIRS Imagery Over Its Predecessors

Key features of VIIRS are its wider swath width and better spatial resolution at swath edge. The VIIRS Imagery swath, at 3000 km, is slightly wider than AVHRR and significantly wider than the 2300 km swath width of MODIS. An example of the impact of the wider swath with VIIRS is seen in Figure 2a, a comparison of the swath widths for VIRIS and MODIS, as plotted across the eastern U.S., covering about half of the width of the continental U.S. For a comparison of the spatial resolution of pixels at swath edge, image zooms (circled in white) from Figure 2a are provided in Figure 2b. The better spatial resolution of VIIRS over MODIS (~1.5 km versus ~ 5 km) at swath edge is clear.

A limitation of MODIS is that the adjacent orbits do not overlap equatorward of 30° latitude, causing data gaps in daily worldwide composites created from MODIS imagery. Such gaps are not seen in VIIRS global composites. This improvement in coverage was the result of one of the requirements for VIIRS Imagery that images of every part of the Earth be refreshed at least every 12 h. A significant advantage of this better


©2014. American Geophysical Union. All Rights Reserved.

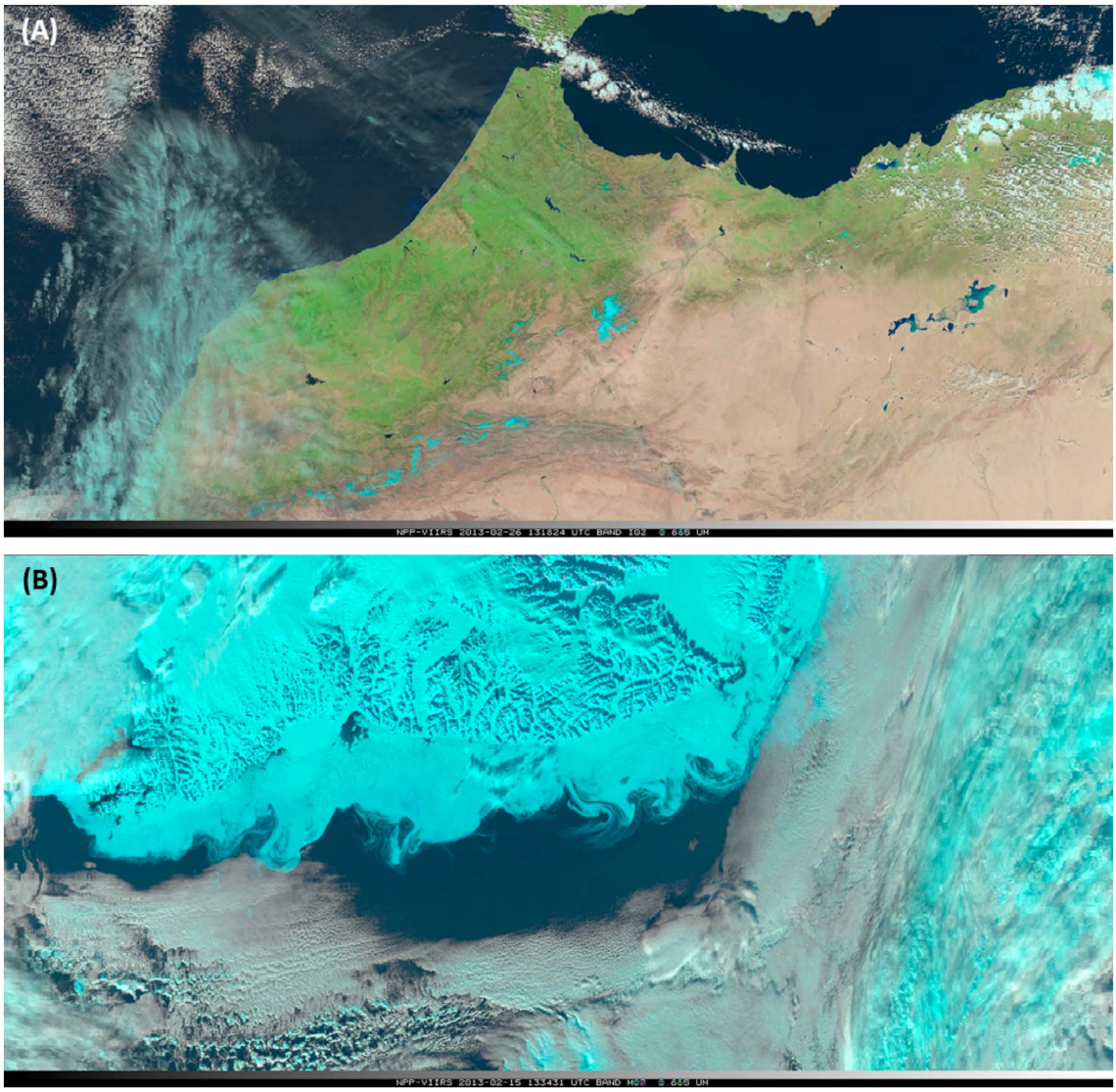


**Figure 1.** (a) An example of a natural color image combination of VIIRS bands M10 (1.61 μm), M7 (0.865 μm), and M5 (0.672 μm), respectively, at 750 m spatial resolution. Only the center portion of this VIIRS granule over the Strait of Gibraltar from 26 February 2013 at 1318 UTC is shown. This multispectral image combination shows the ability to discriminate between many types of image features, ranging from ground cover (vegetated in green versus bare ground in tan/brown versus snow cover in cyan) as well as cloud type (lower level liquid water clouds in white versus thin ice clouds in cyan). (b) Another example of a natural color image combination of VIIRS bands I3 (1.61 μm), I2 (0.865 μm), and I1 (0.64 μm), respectively, at 375 m spatial resolution. Only the center portion of this VIIRS granule from 15 February 2013 at 1334 UTC off of SE Greenland is shown. This image product shows the ability of high-resolution imagery to determine sea ice extent and ice edges using false color imagery.

coverage is that persistent weather features, such as tropical cyclones, are always scanned 2 times per day with VIIRS but may be missed at times by MODIS.

The VIIRS instrument design allows a variable number of subpixel elements to be aggregated into single pixels. In the VIIRS sensor this capability is used to generate I and M band pixels with near-rectangular sample spacing on the ground. To accomplish this, many different aggregation modes are used during the course of the cross-track sensor scan. Since the subpixel aggregation is an additive process, the total number of subpixels aggregated to create each pixel appears as a factor in the radiometric gain of the pixel. At nadir, three detector footprints are aggregated to form a single VIIRS pixel. Moving along the scan away from nadir, the detector footprints become larger both along track and along scan, due to geometric effects and the curvature of the Earth. At 31.59° in scan angle, the aggregation scheme is changed from 3 × 1 to 2 × 1. A similar switch from 2 × 1 to 1 × 1 aggregation occurs at 44.68°. The VIIRS scan consequently exhibits a pixel


©2014. American Geophysical Union. All Rights Reserved.

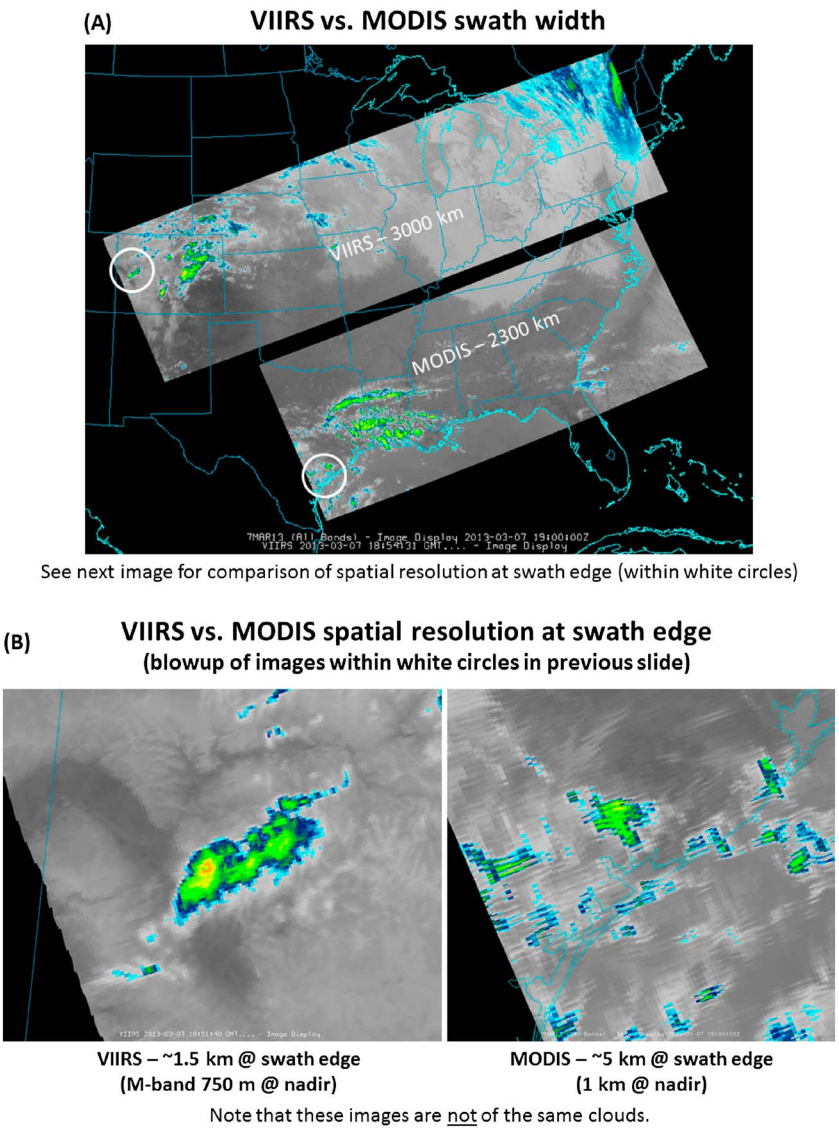


**Figure 2.** (a) Comparison of the swath widths of VIIRS versus MODIS in the longwave infrared (band M15 versus band 31, respectively), showing that the 3000 km wide VIIRS swath stretches across about half of the continental U.S., compared to only about a third for MODIS. (b) Comparison of the spatial resolution of VIIRS versus MODIS at swath edge for the circled-in-white regions, showing that much better VIIRS resolution. (Note, however, that the circles feature different clouds and that the MODIS image has not been corrected for bow tie effects.)

growth factor of only 2 both along track and along scan, compared with a growth factor of 6 along scan which would be realized without the use of the aggregation scheme. This scanning approach allows VIIRS to provide imagery at 800 m resolution or finer globally for the M bands, with 375 m resolution at nadir for the I bands.

Figure 3 shows a comparison of enhanced (and Rayleigh-corrected) true color images from MODIS and VIIRS for a blowing dust event in eastern Colorado on 11 January 2013. For both VIIRS, on the left, and MODIS, on the right, the dust storm was near the edge of swath, allowing a comparison of the capabilities of the two instruments at similar scan angles. Although the MODIS spatial resolution at nadir is better at 500 m (250 m for the red band) versus 750 m for the equivalent true color M bands of VIIRS, there is a clear advantage of having complete coverage of the Earth and higher spatial resolution at swath edge with VIIRS compared to MODIS. Some significant hazard events near swath edge might either be presented at much degraded spatial resolution or missed entirely by MODIS.


©2014. American Geophysical Union. All Rights Reserved.

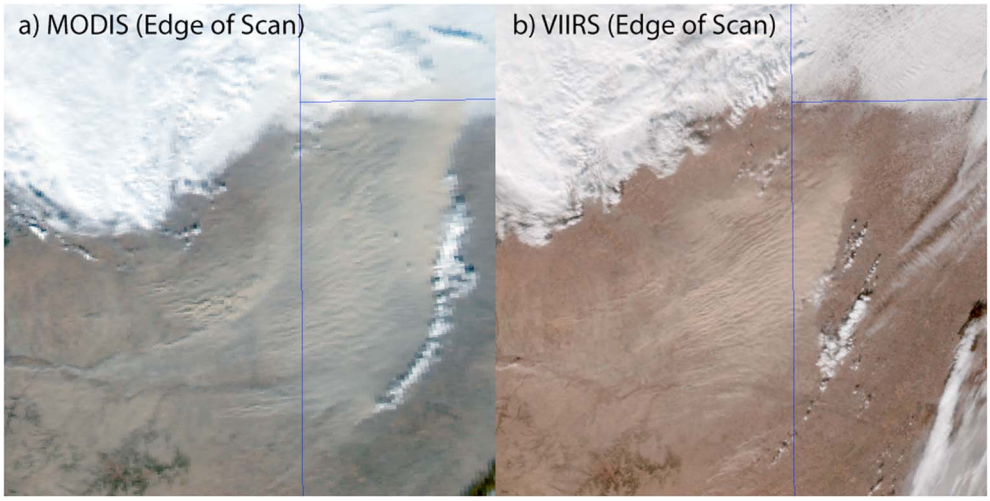


**Figure 3.** (a) MODIS enhanced true color image of blowing dust in eastern Colorado on 11 January 2013 at 2035 UTC. Note the decreased detail of features on the right side of the image, near the edge of the MODIS swath, where the spatial resolution is about 3 km, compared to 500 m resolution at nadir. Features on the right side are adjusted for bow tie effects, the spread in size of pixels with increasing scan angles. (b) VIIRS enhanced true color image of the same blowing dust storm in eastern Colorado as seen at 1926 UTC. The left side of this VIIRS image is near the edge of swath but at about the same viewing angle as the MODIS image. At swath edge the spatial resolution is about 1.5 km, only double the 750 m resolution at nadir for the VIIRS M bands, because features are not compressed in the direction of the scan due to the use of extra sensors that are employed.

## 4. The Identification and Correction of Imagery Issues

The evaluation of VIIRS Imagery is the responsibility of the VIIRS EDR Imagery Team, but VIIRS instrumental and calibration issues are the responsibility of the VIIRS sensor data record (SDR) Team. Most of the issues with the non-NCC EDR Imagery bands have been relatively minor. Some of these issues were rather easily and quickly resolved. The minor issues are not covered here. Rather, a limited number of the more significant imagery problems are presented and their solutions explained.

A significant issue affecting all Imagery EDRs was missing triangles of data due to the remapping of the Imagery SDRs onto the GTM projection grid. Given the constant motion of the satellite, the path of each scan of the instrument is not perpendicular to the satellite track. The GTM projection maps each scan line onto lines perpendicular to the satellite track. A consequence of this is that the lower left and upper right corners of each EDR granule (relative to the motion of the satellite) require scan lines from the previous and subsequent SDR granules, respectively, to fill in these areas. Early production of imagery sometimes created the EDR granules before data from the adjacent SDR granules were available. This resulted in the EDR granule not having access to the radiances from adjacent SDRs. When this occurred, areas of "missing" fill values would be inserted into the granule where the SDR data were not available. These areas were generally triangular in shape (Figure 4). The solution to this problem was twofold: the Imagery EDR processing was slightly delayed to allow more time for adjacent granules to be present and the more significant fix was an improvement in the ground system that minimized delays in receiving the SDR data, almost entirely preventing the missing triangles.

The following section will cover NCC Imagery issues, which were far more significant than any of the non-NCC Imagery problems.

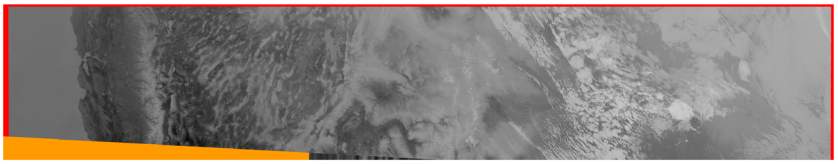

**Figure 4.** An example of a VIIRS EDR granule with a triangular area of missing values, due to the processing of the EDR before the adjacent SDR data were available to provide the missing radiances. Data array values with "N/A Fill" are highlighted as red. Missing fill values are highlighted as orange.


©2014. American Geophysical Union. All Rights Reserved.

**Table 2.** Differences Between DNB and NCC Imagery

| Product | xDR | Units | Mapping |
|---|---|---|---|
| DNB | SDR | Radiances | Raw |
| NCC | EDR | Pseudo-albedos | GTM |

## 5. Production of NCC From DNB Imagery

Until recently, visible band low-light imagery was only provided operationally by the Operational Linescan System (OLS) on board the DMSP spacecraft. OLS nighttime visible imagery spatial resolution is nominally ~2.8 km. The OLS terminator imagery is capable of sensing radiances that span 6–7 orders of magnitude providing the ability to detect atmospheric conditions across the terminator down to clouds illuminated by partial moon conditions [*Elvidge et al.*, 1997]. Viewing imagery that spans this dynamic range is impossible from a single-gain setting. In order to increase this range, the OLS Gain Management Algorithm (GMA), implemented on board the OLS analog signal processor, applies a Gain Value Versus Scene Solar Elevation (GVVSSE) table that adjusts the detected radiance to provide imagery that is nearly constant in contrast [*Lieske*, 1993; *Imagery ATBD*, 2011]. The objective of the GMA is to produce daytime and nighttime imagery that is almost indistinguishable for day-through-terminator solar zenith angles ranging from 0 to 105°. Modeled bidirectional reflectance distribution function (BRDF) effects are also accounted for in both the GVVSSE and Gain Value Versus Scene Lunar Elevation (GVVSLE) tables. In terms of the BRDF functions, they do not partition the function by surface type or latitude. The BDRFs represent the mean reflectance or scattering of the Earth surface and atmosphere (e.g., clouds) and are a function of solar and lunar zenith, solar and lunar azimuth, and relative solar-to-sensor azimuth (and relative lunar azimuth) angles. This adjustment must be done on board because the instrument cannot simultaneously digitize three gain stages (low, middle, and high) with only 6 bits quantization. Thus, the sensor must sequentially navigate through each stage and then apply the GVVSSE/GVVSLE adjustment via the onboard GMA.

The VIIRS DNB is able to detect radiances that span a dynamic range of over 7 orders of magnitude through its spectral response that nominally spans 500–900 nm. The DNB is able to simultaneously digitize four gain stages at superior radiometric resolution: low gain stage (13 bits), middle gain stage (13 bits), and two redundant high gain stages (HGS, 14 bits); the redundancy in HGS (A and B) serves to filter out data that correspond to high-energy particles striking the VIIRS focal plan array. Depending on the level of light in the scene, the appropriate (unsaturated) gain stage is used to optimize sensitivity and avoid saturation. Because these stages can be digitized simultaneously on board, there is the flexibility to apply the GVVSSE/GVVSLE adjustment on the ground. This provides the capability to make algorithm and/or look-up table (LUT) changes via ground software changes. The GMA heritage is preserved for the VIIRS NCC algorithm, however, with some updates to account for the DNB's ability to sense atmospheric conditions in moonless conditions [*Liang et al.*, 2013].

To summarize, the production of NCC Imagery is complex and only approximates an actual albedo, thus the term "pseudo-albedo." The albedos are mapped into the same GTM grid used by the M band Imagery. Table 2 is provided as a summary of differences between the primary characteristics (units and mapping) of DNB and NCC Imagery.

### 5.1. Limited NCC EDR Imagery Production

An early discovered issue was the lack of NCC Imagery under low-light conditions. While NCC Imagery is only specified for quarter moon equivalent levels of illumination, it was clear from the DNB imagery that VIIRS could be used to identify clouds and land features under lower light nighttime conditions. However, that low-light imagery was not being made into NCC EDRs by the operational software. An early attempt at decreasing the minimum threshold for DNB radiances, to account for the much lower light levels that were being observed, did not fully resolve the problem. Later, a look-up table (LUT) change was provided by the software developer that allowed NCC production under nearly all illumination conditions.

NCC Imagery is derived from the DNB and accounts for rapidly changing solar or lunar illumination conditions that often increase the difficulty of a user to determine the feature they are seeking (i.e., clouds). The DNB is composed of a three-stage charge-coupled device to account for the wide-ranging reflectivities from daytime to nighttime/new moon conditions. The NCC algorithm uses the DNB reflectances and determines a pseudo-albedo by modeling the solar and lunar radiance for each pixel. The algorithm preserves heritage from the OLS Gain Management Algorithm (GMA) through the use of look-up tables (LUTs) designed to mimic the GMA.


©2014. American Geophysical Union. All Rights Reserved.

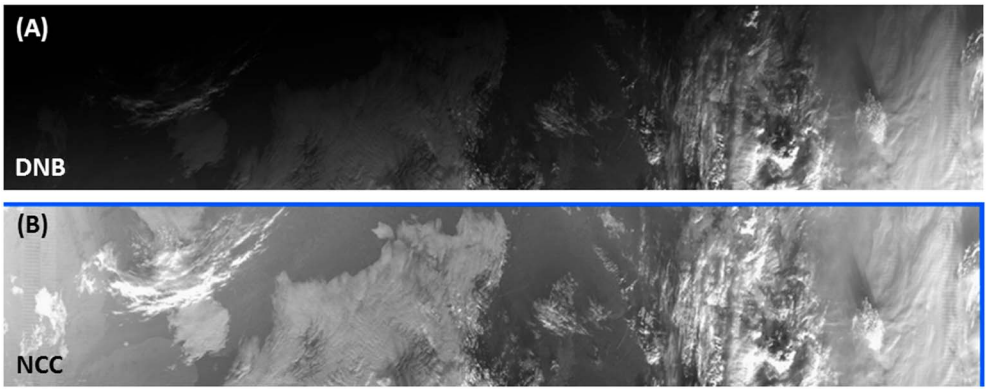


**Figure 5.** (a) A DNB (SDR) granule that crosses the day/night terminator (with bow tie deleted pixels removed). (b) The associated NCC (EDR) granule (with fill values highlighted in blue). Neither image has been mapped.

An example of the SDR and associated EDR is shown in Figure 5. The goal of the NCC EDR is to reduce the observed range of DNB radiances by converting it to a quantity with a smaller range of values (i.e., pseudo-albedo) to create images with nearly constant contrast across the scenes. By this process, nighttime images of clouds should, in principle, appear very similar to solar reflectance-based daytime imagery.

The most troublesome issue with NCC Imagery is a stray light issue that caused imagery at higher latitudes and under low-light conditions to appear washed out due to sunlight (either direct beam or reflected off portions of the spacecraft) infiltrating the VIIRS instrument when the S-NPP spacecraft is under direct illumination by the Sun at specific geometries. This issue is exacerbated by the fact that the DNB is so sensitive to extremely low levels of radiation that the existing protection (baffling) for stray light was insufficient. This problem is most prominent at certain satellite orientations with respect to the Sun or places in the satellite's polar orbit. A software correction for stray light-affected DNB imagery has been developed by Northrop Grumman and was implemented in mid-2013 [*Mills et al*., 2013; *Liang et al*., 2013]. Unfortunately, because no hardware fix is being implemented to further remove extreme low levels of stray light, this problem will likely persist into the first of the JPSS series. However, the implemented

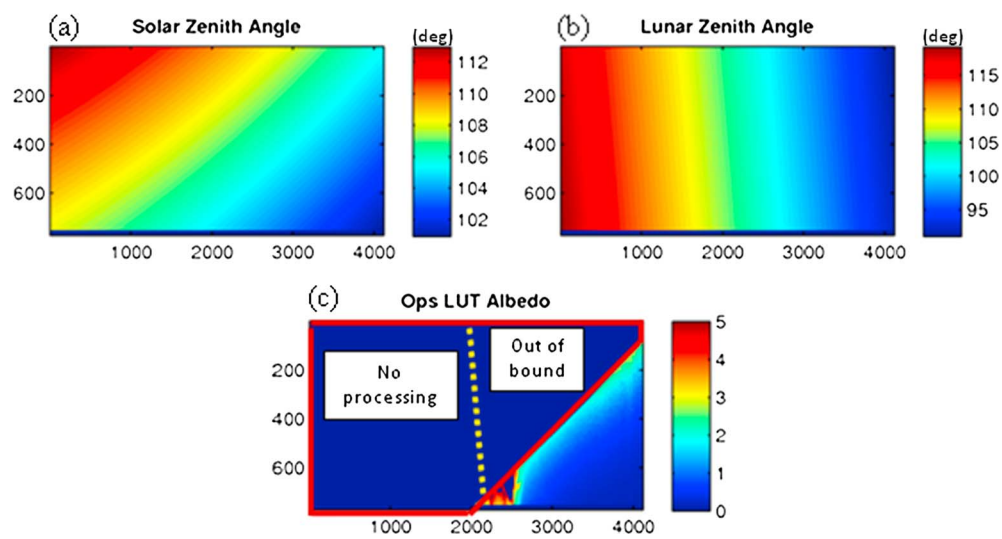


**Figure 6.** (a) Solar zenith angle and (b) lunar zenith angle map of an NCC granule observed on 12 June 2012 between 00:10 and 00:12 UTC on orbit b03229. (c) The operationally produced NCC pseudo-albedo map. To the right of the dotted yellow line are the fill values due to an "out of bounds" condition, and to the left are fill values result from the NCC algorithm not processing beyond solar and lunar zenith angles beyond 105°.


©2014. American Geophysical Union. All Rights Reserved.

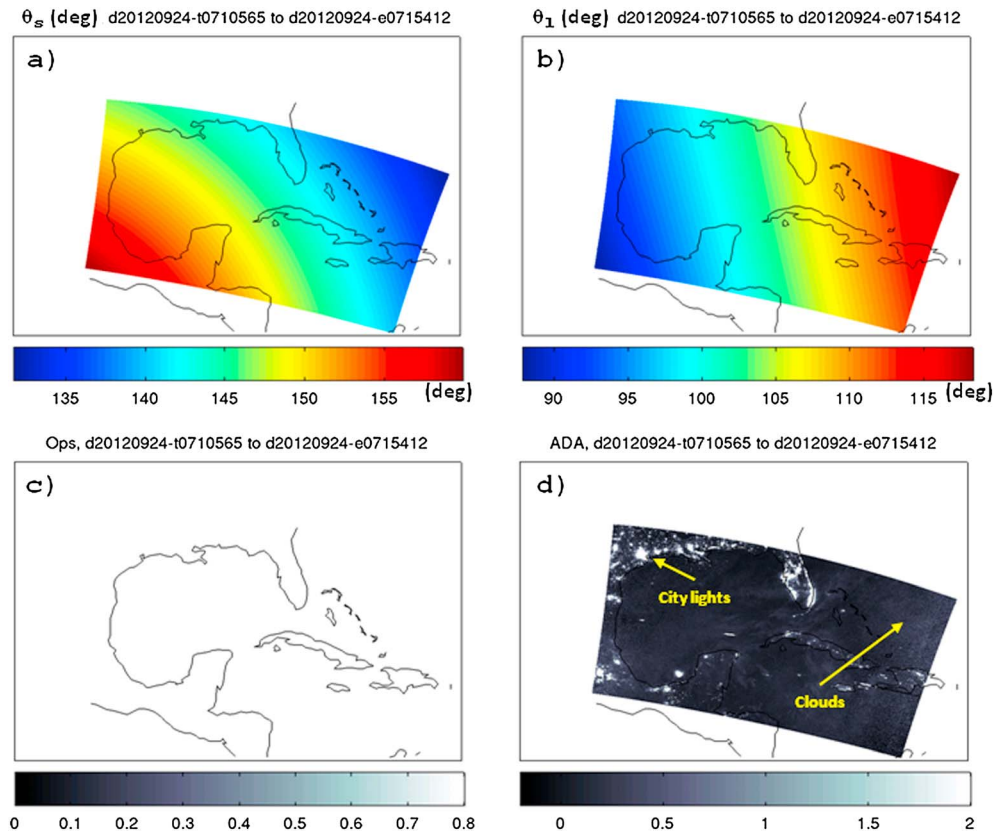


**Figure 7.** VIIRS NCC data taken on 24 September 2012 between 07:10 and 07:15 UTC (near first quarter moon condition). (a) Solar zenith angle ($\theta_s$), (b) lunar zenith angle ($\theta_l$), (c) the current operationally produced NCC pseudo-albedo, and (d) the new pseudo-albedo that would result with the algorithm threshold and gain adjustments.

solution will be monitored, and attempts will be made to reduce the effects of stray light during the lifetime of these spacecraft. For more about stray light, see section 5.1.2.

### 5.1.1. Algorithm Design and LUT Thresholds

The Interface Data Processing Segment has been operationally producing properly calibrated DNB SDRs since March 2012 and valid daytime NCC Imagery as well. However, valid nighttime NCC Imagery production was limited to a time period of about 1 week around the full moon of each month. Furthermore, there was no imagery produced beyond solar zenith ($\theta_s$) and lunar zenith ($\theta_l$) angles of 105° since the algorithm was originally intended to produce imagery for daytime/nighttime and through the solar/lunar terminators. The following are the nominal conditions that lead to no imagery, i.e., fill values, in NCC production: (1) $\theta_s$ and $\theta_l > 105°$ (algorithm exclusion, FILL = 65535), (2) DNB radiance ($L_{DNB}$) is negative (scaling out of bounds, FILL = 65528), and (3) NCC pseudo-albedo ($\alpha$) falls outside the (0–5) range (scaling out of bounds, FILL = 65528).

Condition (1) was an original design limitation that legislated NCC would not be produced beyond the solar and lunar terminators. Condition (3) results from either negative radiances (Condition (2)), which occur for very dark scenes around new moon (moonless) conditions or $\alpha$ becoming too high. The pseudo-albedo becomes large for dark moonless (or near moonless) pixels, i.e., large $\theta_l$, that contain auroras, bright city lights, lightning flashes, fires/gas flares, ship lights, or other bright man-made illumination sources. However, another cause for high $\alpha$ values arises when $\theta_s$ exceeds 105° but $\theta_l$ is close to 105°. This situation is observed in the NCC granule discussed below.

Figure 6 shows an operational NCC granule for data observed on 12 June 2012 between 00:10:42 and 00:12:13 UTC. The granule shows regions where both $\theta_s$ and $\theta_l > 105°$ (Figures 6a and 6b). The resulting NCC image (Figure 6c) shows fill values for $\theta_s > 105°$ indicated by the red bordered region. The region to the left of the yellow dotted line contains fill values resulting from the "algorithm exclusion" condition with $\theta_s$ and


©2014. American Geophysical Union. All Rights Reserved.

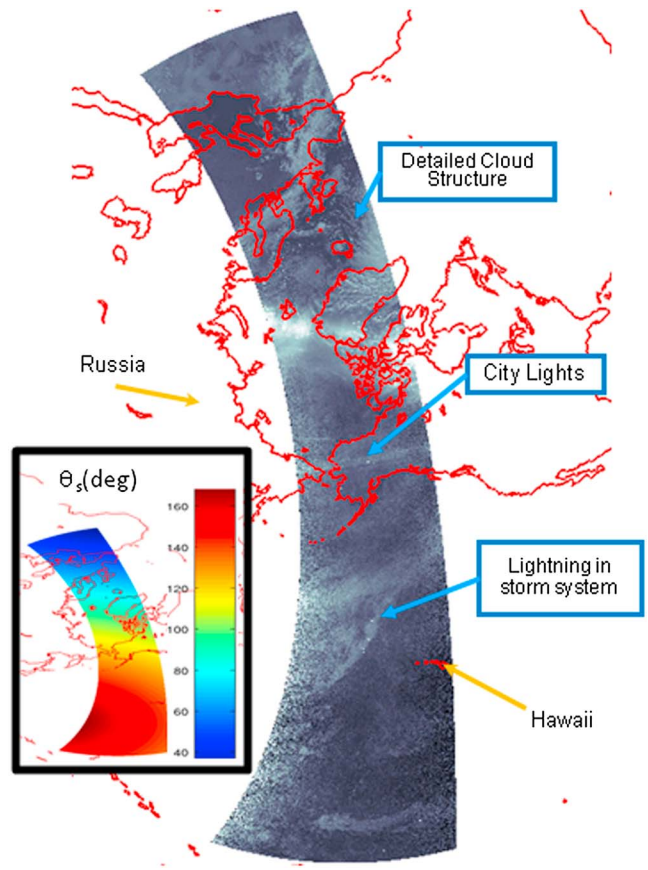


**Figure 8.** Thirty-two continuous NCC granules, with new LUT threshold and gain adjustments, taken from 19 October 2012 from 12:10 to 13:00 UTC. The granules span day and night as indicated by the solar zenith angle ($\theta_s$) color map. Features such as detailed clouds, city lights, and a storm system are highlighted. Maps are on an equidistant azimuthal projection.

$\theta_l > 105°$. The area to the right of the yellow dotted line contains fill values resulting from the "scaling out of bounds" condition. Thus, it is necessary to extend both $\theta_s$ and $\theta_l$ thresholds out to 180°.

#### 5.1.2. Stray Light Contamination

In addition to the stringent thresholds on $\theta_s$, $\theta_l$, and $\alpha$, stray light contamination impacts NCC as well. New moon data (i.e., data around moonless nights) are used to derive gain, i.e., the GVVSSE and GVVSLE tables that adjust the DNB radiances to compute $\alpha$. Approximately 25% of nighttime scenes, including terminator scenes, are contaminated with stray light [*Mills et al.*, 2013; *Liang et al.*, 2013]. The stray light likely results from leakage of light entering the VIIRS scan cavity through the nadir (Earth viewing) door and solar diffuser. It manifests itself as a gray haze in the SDR imagery and shifts in geolocation as a function of season. To correctly derive the GVVSSE and GVVSLE the stray light must be correctly characterized and removed.

#### 5.1.3. Airglow and Its Influence on the GVVSSE/GVVSLE LUTs

One other aspect of the $L_{DNB}$ distribution that must be accounted for is airglow [*Ingham*, 1971]. An assortment of chemiluminescent reactions, predominately those involving excited-state hydroxyls, atomic and molecular oxygen, and atomic sodium, account for emissions in the visible and near-infrared (stronger), with peak emissions near the mesopause (~87 km). The airglow generalizes a light production process that has three subcategories: dayglow, twilight glow, and nightglow. For the purposes of NCC the main process that can be observed from an imagery perspective is the nightglow. The DNB has been shown to be sensitive enough to sense both the direct emission and cloud/surface reflectance of this faint nightglow signal on moonless nights, with radiances of order of $10^{-10}\,\mathrm{W \cdot cm^{-2} \cdot sr^{-1}}$ [*Miller et al.*, 2012]. This leads to poor NCC Imagery because the GVVSSE/GVVSLE LUTs were generated assuming an exponential falloff of radiance beyond twilight. The observed nightglow in the DNB radiances acts as an extra source of radiance and must be accounted for to produce high-quality NCC Imagery.


©2014. American Geophysical Union. All Rights Reserved.

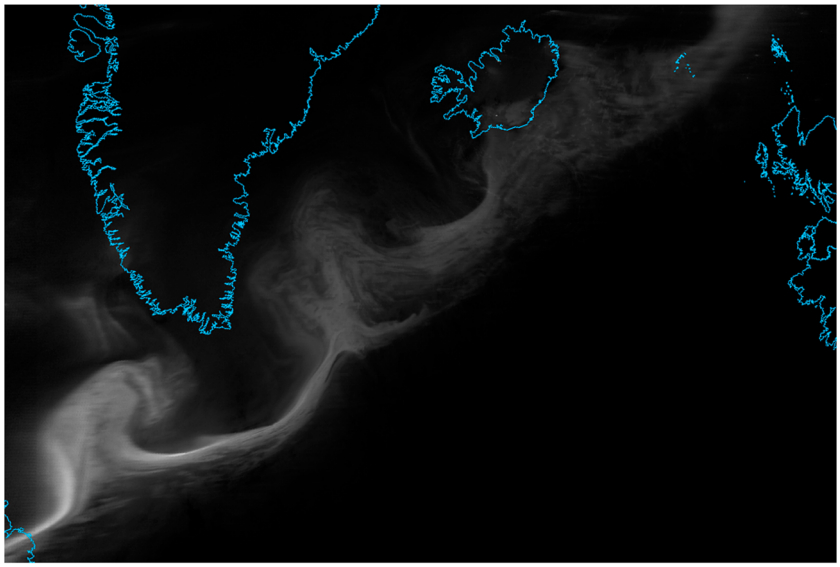

**Figure 9.** An example of an aurora seen in the DNB over the North Atlantic Ocean at 04:19 UTC on 14 November 2012. The aurora stretches from Newfoundland (lower left corner) off the coast of Greenland and Iceland to just north of the Shetland Islands (upper right corner).

### 5.2. Corrected NCC Imagery and Its Utility

After adjusting the algorithm thresholds, removing stray light contamination [*Mills et al*., 2013; *Liang et al*., 2013], and accounting for the observed nightglow, the NCC EDR algorithm produces imagery for all solar and lunar conditions. Figure 7 shows three continuous NCC night (see $\theta_s$ and $\theta_l$ in Figures 7a and 7b respectively) granules taken near a first quarter moon on 24 September 2012 from 07:10 to 07:15 UTC. The original operational product (Figure 7c) shows no imagery because the algorithm does not produce imagery for $\theta_s$ and $\theta_l > 105°$. There is no imagery for $\theta_s > 105°$ and $\theta_l \leq 105°$ because $\alpha$ becomes much larger than 5. Figure 7d shows the resultant NCC Imagery after the algorithm thresholds, and gain adjustments were applied. City lights and faint cloud features are observable.

One of the most useful features of NCC, and its originally intended purpose, is to identify atmospheric features in the vicinity of the terminator. However, since the NCC Imagery now extends to $\theta_s > 105°$, it is possible to observe atmospheric features throughout the day and night. Figure 8 shows 32 contiguous NCC granules taken from 19 October 2012 between 12:10 and 13:00 UTC (near new moon condition). City lights, detailed cloud structures, and storm systems can be observed simultaneously; the transition between day and night is almost indiscernible (Toward the southern portion of the map, the image looks more "grainy" or noisy because the radiances of the night granules are near the noise floor.).

The updated thresholds and GVVSSE/GVVSLE adjustments became operational in mid-2013 and are currently providing high-quality NCC Imagery from S-NPP. Clearly, from an imagery standpoint, this makes it possible to simultaneously observe day and night atmospheric structures on a global scale. From a weather forecasting standpoint, it is possible to forecast clouds more accurately because the global cloud structure is visible both day, night, and around the terminator.

## 6. A Survey of VIIRS Imagery and Its Uses

VIIRS Imagery has a multitude of uses, ranging from land and ocean surfaces to the upper atmosphere. As it is not feasible to cover all known uses, a few representative examples will be shown. Additional examples are discussed in *Hillger et al*. [2013].

The DNB is capable of observing the aurora, an upper atmosphere phenomenon, at night during any phase of the moon. An example of the aurora over the North Atlantic Ocean near a new moon is shown in Figure 9. It has been demonstrated that the DNB is capable of observing rapid motions of the aurora that are related to fluctuations in the Earth's magnetic field [*Seaman and Miller*, 2013].


©2014. American Geophysical Union. All Rights Reserved.

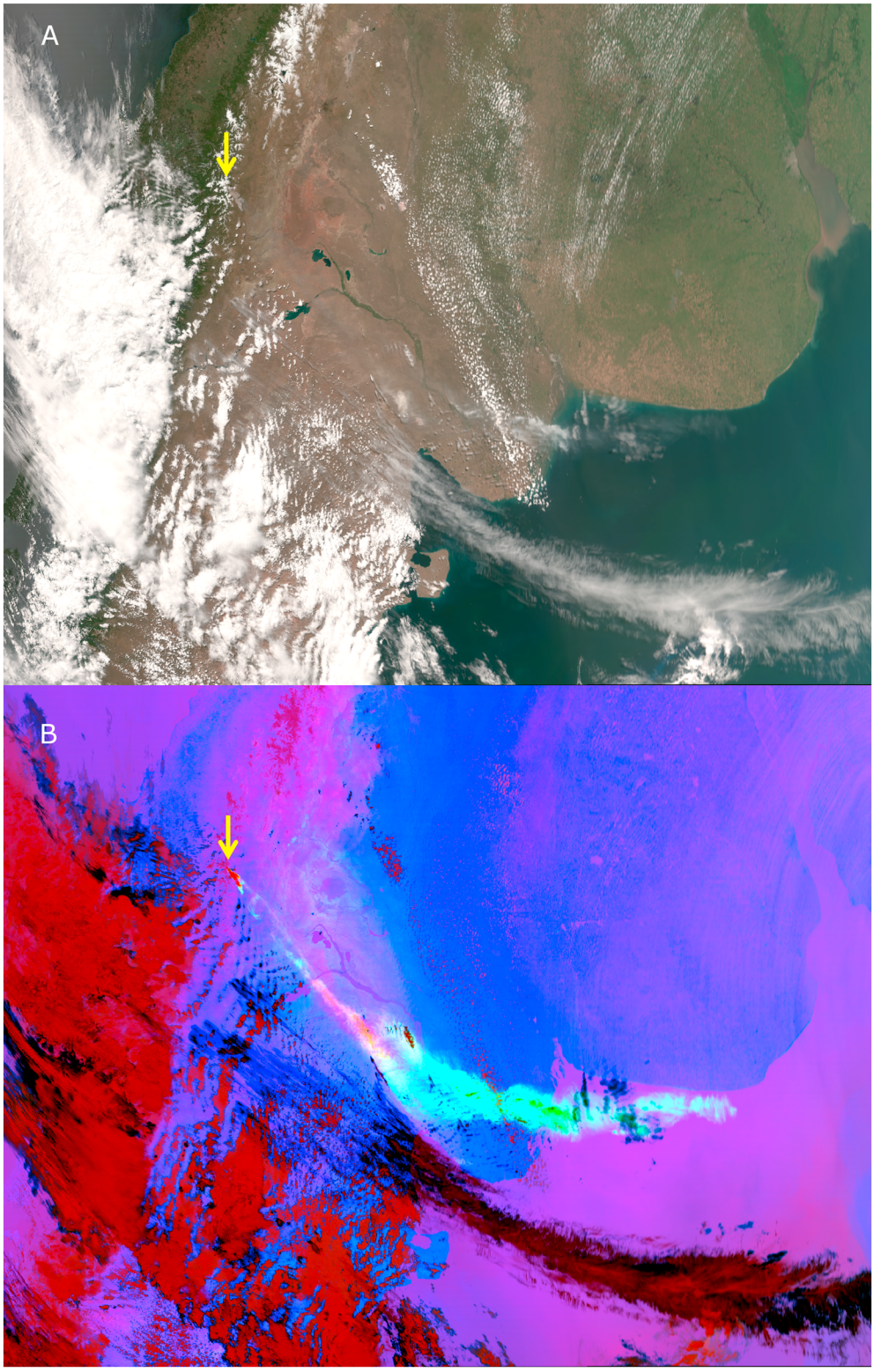


**Figure 10.** (a) True color image and (b) Dust RGB image of the Copahue volcanic eruption of 22 December 2012 at 18:38 UTC. The yellow arrows indicate the location of the volcano. The Dust RGB composite is sensitive to the $SO_2$ emitted by the volcano. The $SO_2$ plume is not visible in the true color image (Figure 10a) yet is seen (in blue green) extending over the Atlantic Ocean in the false color RGB composite (Figure 10b). The optically thick portion of the ash cloud appears near the volcano as brown in Figure 10a and red in Figure 10b.


©2014. American Geophysical Union. All Rights Reserved.

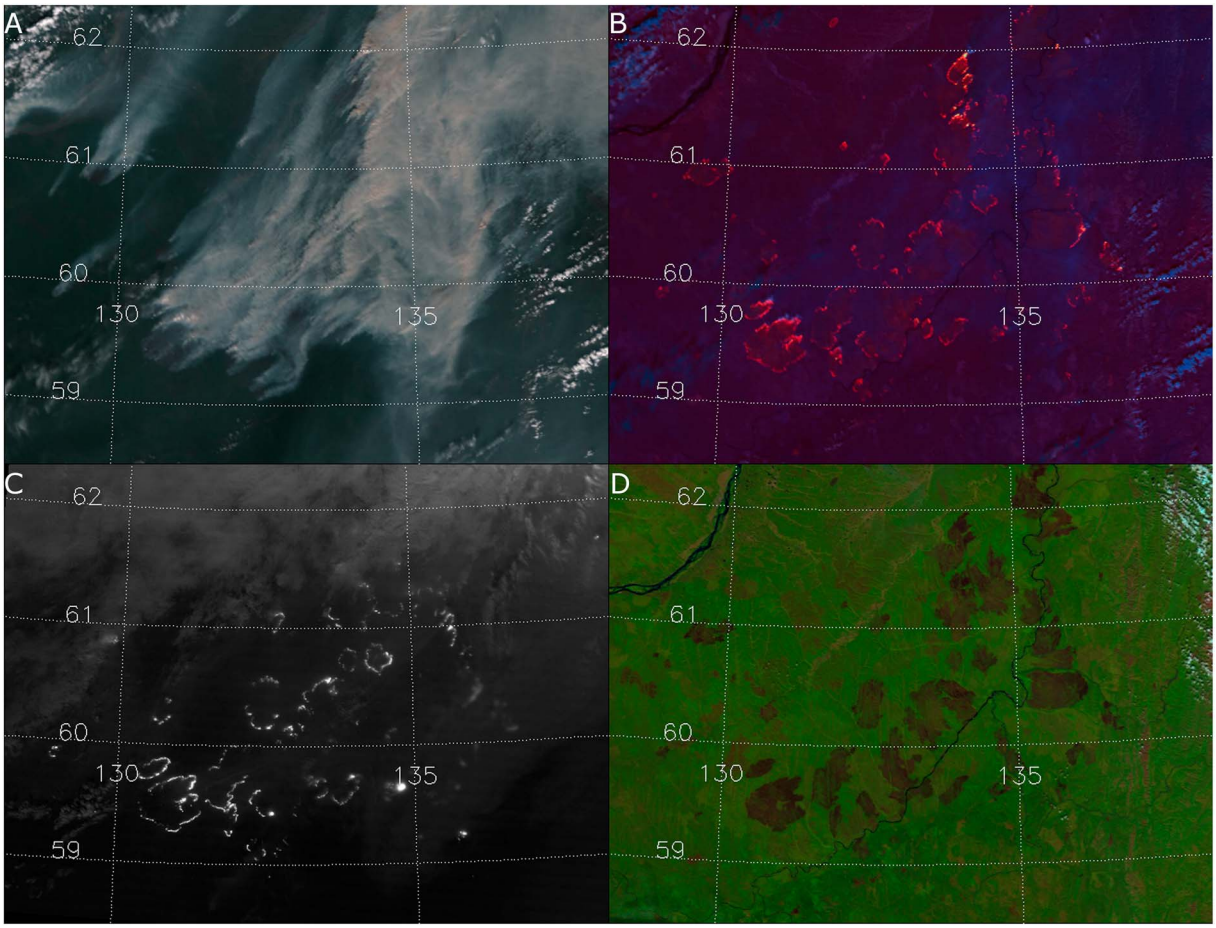


**Figure 11.** A sequence of images of numerous wildfires in Siberia. (a) Smoke dominates the true color image from 4 August 2012 at 02:38 UTC. (b) The Fire Temperature RGB image, also from 4 August 2012 at 02:38 UTC, shows the hot spots associated with the actively burning fires. (c) The DNB detects the active fires as well as the moonlit smoke and clouds in this nighttime image from 4 August 2012 at 16:26 UTC. (d) The natural color image from 7 August 2012 at 03:22 UTC shows the effect of the fires on vegetation health, with dark brown burn scars clearly visible.

VIIRS band M14 (8.55 μm) is sensitive to absorption by sulfur dioxide ($SO_2$) gas, a source of which is volcanic activity. Explosive volcanic eruptions send plumes of $SO_2$ and ash into the atmosphere, making detection of $SO_2$ useful for the detection of volcanic ash [*Kreuger et al*., 2009]. Volcanic ash is a major hazard to aviation. Figure 10 shows VIIRS images of the Copahue volcano on the border between Chile and Argentina, a few hours after it erupted on 22 December 2012. Figure 10a shows the "true color" composite of RGB bands M5 (0.672 μm), M4 (0.555 μm), and M3 (0.488 μm), while Figure 10b shows the associated "Dust RGB" composite. The volcano and ash cloud are highlighted by the yellow arrows. The Dust RGB composite is another featured imagery product from Meteosat [*Lensky and Rosenfeld*, 2008] that may be applied to VIIRS. The red component is the brightness temperature difference between M16 (12.0 μm) and M15 (10.7 μm), the green component is the brightness temperature difference between M15 and M14, and the blue component is the brightness temperature of M15. The $SO_2$ absorption present in M14 highlights the plume that likely contains ash particles and is effectively invisible in the true color image.

Figure 11 shows a sequence of VIIRS images related to a large area of wildfires that occurred in Siberia in early August 2012. Figure 11a shows a true color image from 02:38 UTC on 4 August 2012. Optically thick smoke plumes cover the majority of the scene. Figure 11b shows a false color RGB composite, also from 02:38 UTC on 4 August 2012 that highlights pixels with actively burning fires. This composite, which we refer to as the "Fire Temperature RGB," contains radiances from M10 (1.61 μm, blue), M11 (2.25 μm, green), and M12 (3.74 μm, red). Hot spots appear red, orange, yellow, or white, depending on their radiative temperature, with white representing the most intense fires. As shown in Figure 11b, the Fire Temperature


©2014. American Geophysical Union. All Rights Reserved.

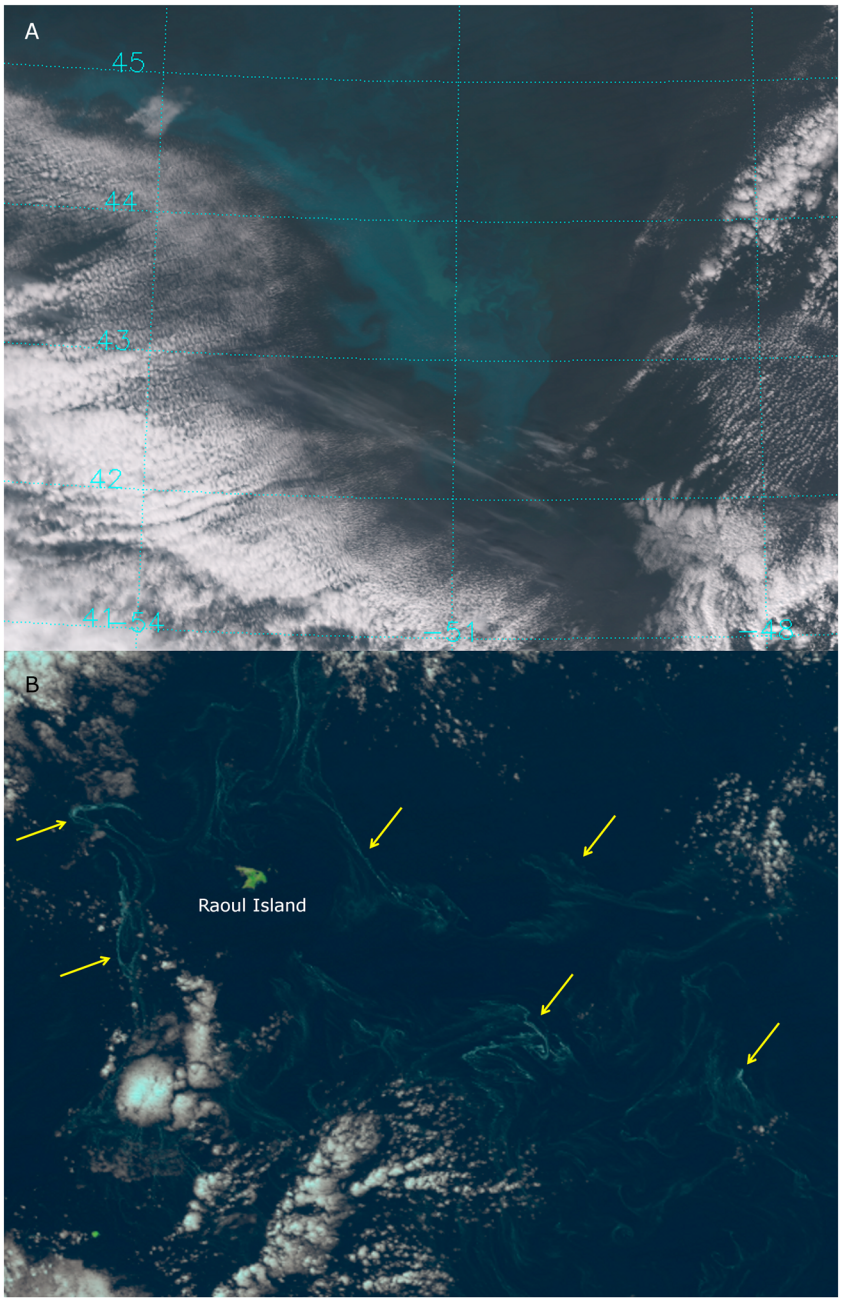


**Figure 12.** Examples of VIIRS Imagery uses for ocean applications. (a) True color image of a phytoplankton bloom off the coast of Newfoundland, Canada, on 6 March 2013 at 15:52 UTC. The southeast tip of Newfoundland is outlined under the clouds near the upper left corner of the image. (b) Natural color image of pumice rafts in the South Pacific Ocean near Raoul Island, approximately 1000 km northeast of New Zealand, on 27 August 2012 at 01:40 UTC. The yellow arrows identify various pumice rafts, indicating the extensive area containing pumice following an underwater eruption of the Havre Seamount on 18 July 2012.

RGB is capable of identifying hot spots despite the copious amounts of smoke. Figure 11c shows the DNB image from the following night (4 August 2012 at 16:26 UTC). The light emitted by the active fires is clearly visible. The reflection of moonlight off of smoke and clouds is also visible. Figure 11d shows the natural color image from 7 August 2012 at 03:22 UTC after the fire activity greatly diminished. Dark brown burn scars are clearly visible within the strong green vegetation signal from the surrounding boreal forest. This example demonstrates several ways VIIRS may be used for fire applications. VIIRS is capable of detecting smoke and


©2014. American Geophysical Union. All Rights Reserved.

active fire hotspots, plus the natural color imagery is useful for monitoring vegetation health in the aftermath of fires.

Finally, Figure 12 shows two examples of ocean applications of VIIRS. Figure 12a is a true color image of a phytoplankton bloom in the North Atlantic Ocean off the coast of Newfoundland, Canada. Phytoplankton blooms may both help and harm the health of ocean ecosystems [*McKibben et al.*, 2012] and are an important component of the global carbon cycle [*Field et al.*, 1998]. Figure 12b is a natural color image of pumice rafts produced by an underwater eruption of the Havre Seamount that occurred on 18 July 2012. The image in Figure 12b, taken 40 days after the eruption, shows the broad area containing floating pumice surrounding Raoul Island in the South Pacific Ocean. Pumice rafts have been shown to be important in the transport of a variety of marine organisms [*Bryan et al.*, 2004, 2012], and VIIRS has the ability to monitor the dispersal of the pumice from its origination.

## 7. Summary and Conclusions

The checkout of VIIRS Imagery quality has been so successful that the non-NCC Imagery has been at the "Provisional" maturity level since early 2013, after having resolved several mostly minor imagery issues. NCC Imagery also reached the provisional stage, arriving there much later in 2013, in spite of early limited use at night under minimal moonlight conditions, as well as a stray light hardware issue for which a software fix is being implemented. Both NCC and non-NCC Imagery have since reached the "Validation 3" maturity level in April 2014 as this manuscript was being prepared.

Besides the imagery examples presented here, there are online sources of VIIRS Imagery. Basic VIIRS granule images and image products, as well as some remapped imagery and products, can be found on an S-NPP VIIRS online display (http://rammb.cira.colostate.edu/ramsdis/online/), and an S-NPP VIIRS Imagery blog (http://rammb.cira.colostate.edu/projects/npp/blog/) with many interesting case studies of the use of VIIRS Imagery is also available. A third site (http://rammb.cira.colostate.edu/projects/alaska/blog/) features specific uses of VIIRS in the Arctic and is titled "Seeing the Light."

**Acknowledgments**
The authors would like to thank the following additional members of the VIIRS Imagery and Visualization Team (http://rammb.cira.colostate.edu/projects/npp/) for their contributions: Tom Lee, Stan Kidder, Debra Molenar, Steve Finley, Renate Brummer, Tommy Jasmin, Tom Rink, William Straka III, Chris Elvidge, Jeff Hawkins, Jeremy Solbrig, Kim Richardson, Keith Hutchinson, Steve Mills, Stephanie Weiss, Ryan Williams, and Tim Schmit (GOES Imagery liaison). Funding for this work was provided by the JPSS Program Office and NOAA/NESDIS/STAR. The views, opinions, and findings contained in this article are those of the authors and should not be construed as an official National Oceanic and Atmospheric Administration (NOAA) or U.S. Government position, policy, or decision.

## References

Bryan, S. E., A. Cook, J. P. Evans, P. W. Colls, M. G. Wells, M. G. Lawrence, J. S. Jell, A. Greig, and R. Leslie (2004), Pumice rafting and faunal dispersion during 2001–2002 in the Southwest Pacific: Record of a dacitic submarine explosive eruption from Tonga, *Earth Planet. Sci. Lett.*, *227*, 135–154.

Bryan, S. E., A. G. Cook, J. P. Evans, K. Hebden, L. Hurrey, P. Colls, J. S. Jell, D. Weatherly, and J. Firn (2012), Rapid, long-distance dispersal by pumice rafting, *PLoS One*, *7*, e40583, doi:10.1371/journal.pone.0040583.

Elvidge, C. D., K. E. Baugh, A. Kihn, H. W. Kroehl, and E. R. Davis (1997), Mapping city lights with nighttime data from the DMSP Operational Linescan System, *Photogramm. Eng. Remote Sens.*, *63*, 727–734.

Field, C. B., M. J. Behrenfeld, J. T. Randerson, and P. Falkowski (1998), Primary production of the biosphere: Integrating terrestrial and oceanic components, *Science*, *281*, 237–240.

Hillger, D., et al. (2013), First-light imagery from Suomi NPP VIIRS, *Bull. Am. Meteorol. Soc.*, *94*, 1019–1029, plus cover images, doi:10.1175/BAMS-D-12-00097.1.

Imagery Algorithm Theoretical Basis Document (ATBD) (2011), Joint Polar Satellite System (JPSS) VIIRS imagery products Algorithm Theoretical Basis Document (ATBD), NASA GSFC JPSS CMO, Joint Polar Satellite System Ground Project, Code 474, 474-00031, 122 pp. [Available at http://www.star.nesdis.noaa.gov/jpss/ATBD.php#S494897.]

Imagery Calibration/Validation Plan (2009), NPOESS Community Collaborative Calibration/Validation Plan for the NPOESS Preparatory Project VIIRS Imagery EDR, NPOESS Integrated Program Office, 18 pp. [Available at http://www.star.nesdis.noaa.gov/jpss/documents/CalVal/CVP_EDR_VIIRS_Imagery_Kopp_Public_Release_Oct2009.pdf.]

Ingham, M. F. (1971), The light of the night sky and the interplanetary medium, *Rep. Prog. Phys.*, *34*, 875–912.

Kreuger, A. J., N. A. Krotkov, K. Yang, S. Carn, G. Vicente, and W. Schroeder (2009), Applications of satellite-based sulfur dioxide monitoring, *IEEE J. Sel. Top. Appl. Earth Obs. Remote Sens.*, *2*, 293–298, doi:10.1109/JSTARS.2009.2037334.

Lee, T. F., S. D. Miller, F. J. Turk, C. Schueler, R. Julian, S. Deyo, P. Dills, and S. Wang (2006), The NPOESS VIIRS day/night visible sensor, *Bull. Am. Meteorol. Soc.*, *87*, 191–199, doi:10.1175/BAMS-87-2-191.

Lee, T. F., et al. (2010), NPOESS: Next-generation operational global Earth observations, *Bull. Am. Meteorol. Soc.*, *91*, 727–740, doi:10.1175/2009BAMS2953.1.

Lensky, I. M., and D. Rosenfeld (2008), Clouds-Aerosols-Precipitation Satellite Analysis Tool (CAPSAT), *Atmos. Chem. Phys.*, *8*, 6739–6753, doi:10.5194/acp-8-6739-2008.

Level 1 Requirements Document (L1RD) (2013), Joint Polar Satellite System (JPSS) program Level 1 Requirements Document–Final, version 1.7, DoC/NOAA/NESDIS, 32 pp.

L1RD Supplement (2013), Joint Polar Satellite System (JPSS) Level 1 Requirements–Supplement–Final, version 2.9, DoC/NOAA/NESDIS, 148 pp.

Lewis, J. M., D. W. Martin, R. M. Rabin, and H. Moosmüller (2010), Suomi: Pragmatic visionary, *Bull. Am. Meteorol. Soc.*, *91*, 559–577, doi:10.1175/2009BAMS2897.1.

Liang, C. K., S. Mills, B. I. Hauss, and S. D. Miller (2013), Improved VIIRS day/night band imagery with near constant contrast, *IEEE Trans. Geosci. Remote Sens.*, doi:10.1109/TGRS.2014.2306132.


©2014. American Geophysical Union. All Rights Reserved.

Lieske, R. W. (1993), Technical operating report for Block 5D-3 Operational Linescan System (OLS), Westinghouse Defense and Electronic Systems Center.

McKibben, S. M., P. G. Strutton, D. G. Foley, T. D. Peterson, and A. E. White (2012), Satellite-based detection and monitoring of phytoplankton blooms along the Oregon coast, *J. Geophys. Res.*, *117*, C12002, doi:10.1029/2012JC008114.

Miller, S. D., and R. E. Turner (2009), A dynamic lunar spectral irradiance dataset for NPOESS/VIIRS Day/Night Band nighttime environmental applications, *IEEE Trans. Geosci. Remote Sens.*, *47*(7), 2316–2329, doi:10.1109/TGRS.2009.2012696.

Miller, S. D., S. P. Mills, C. D. Elvidge, D. T. Lindsey, T. F. Lee, and J. D. Hawkins (2012), Suomi satellite brings to light a unique frontier of nighttime environmental sensing capabilities, *Proc. Natl. Acad. Sci. U. S. A.*, *109*(39), 15,706–15,711, doi:10.1073/pnas.1207034109.

Mills, S. P., S. C. Weiss, and C. K. Liang (2013), VIIRS Day/Night Band (DNB) stray light characterization and correction, in *Earth Observing Systems XV*, SPIE Optical Engineering + Applications, San Diego.

Seaman, C. J., and S. D. Miller (2013), VIIRS captures aurora motions, *Bull. Am. Meteorol. Soc.*, *94*, 1491–1493, doi:10.1175/BAMS-D-12-00221.1.


©2014. American Geophysical Union. All Rights Reserved.